A μFE Simulation-based Surrogate Machine Learning Model to Predict Mechanical Functionality of Protein Networks from Live Confocal Imaging

Pouyan Asgharzadeh[a,b,*], Annette I. Birkhold[a,b,1], Zubin Triverdi[a], Bugra Özdemir[c,d], Ralf Reski[c,d,e,2], Oliver Röhrle[a,b,3]

[a] *Institute for Modelling and Simulation of Biomechanical Systems, University of Stuttgart, Stuttgart, Germany*
[b] *Stuttgart Center for Simulation Science (SC SimTech), Stuttgart, Germany*
[c] *Plant Biotechnology, Faculty of Biology, University of Freiburg, Freiburg, Germany*
[d] *Signalling Research Centres BIOSS and CIBSS, Freiburg, Germany*
[e] *Cluster of Excellence livMatS @ FIT - Freiburg Centre for Interactive Materials and Bioinspired Technologies, Freiburg, Germany*

[*] Corresponding author.
Email address: asgharzadeh@imsb.uni-stuttgart.de (Pouyan Asgharzadeh)
URL: http://bit.ly/2Tqx_PA (Pouyan Asgharzadeh)
[1] Currently an employee of Siemens Healthcare GmbH.
[2] ORCID ID: 0000-0002-5496-6711 (Ralf Reski)
[3] ORCID ID: 0000-0002-1934-6525 (Oliver Röhrle)

Abstract

Understanding sub-cellular mechanics is crucial for a better understanding of a variety of biological functions and dysfunctions. A structure-function analysis of the cytoskeletal protein networks provides not only ways to deduce from its structure insights into its mechanical behaviour but potentially also new insights into sub-cellular processes such as mechano-transduction, stiffness-induced cytoskeletal restructuring and stiffness changes, or mechanical aspects of cell-biomaterial interactions. Recently, fluorescence imaging has become a powerful tool to study protein network structures at high resolution. Yet, automated tools for quantitative functional analysis of these complex structures, are missing. These, however, are needed to relate structural characteristics to cellular functionality. Here, we present a machine learning framework that combines 3D imaging and mechanical modelling on the nano scale, enabling prediction of mechanical behaviour of protein networks and the subsequent automatic extraction of structural features of which one can deduce mechanical characteristics. This study demonstrates the method's applicability to investigate the skeleton's functionality of the Filamentous Temperature Sensitive Z (FtsZ) family inside organelles (here, chloroplasts) of the moss *Physcomitrella patens*.

Keywords: surrogate modelling, machine learning, finite element analysis, structure-function relationship, plastoskeleton

1. Introduction

In biology, bio-polymer networks are pervasive as key promoters of strength, support and integrity. This is true irrespectively of its scale, i.e., from the micro-scale of the cytoskeleton to the macro-scale of connective tissues. As cells sense external physical signals and translate them into a cellular responses, cellular mechanics has been proven to be crucial for a wide range of biological functions and dysfunctions. In particular cytoskeletal protein networks exhibit strong structure-function relationships, e.g., the role of microtubule network during mitosis [1], cell movement with the help of actin assembly/disassembly [2] or utilizing intermediate filament networks for stabilizing mechanical stresses [3]. Therefore, investigating the structure of protein networks allows deeper insights into their functionality/dysfunctionality.

In the recent decades, taking advantage of new methodological developments in experimental and computational physics and applying them to biological systems allowed substantial progress in elucidating particular mechanical phenomena to biological function. By such new methods, researchers have shown that mechanical processes convey biochemical signals and are therefore crucial for cell functions including proliferation, polarity, migration and differentiation. Further, connections between the mechanical properties of cells, of its initiation, or of its pathological progression such as it occurs in cancer, were established, e.g., by Guck et al. [4] or Suresh et al. [5]. Suresh, for example, showed that the elasticity of malaria-infected red blood cells exhibit higher stiffness than healthy ones [6]. Mendez et al. [7] or Liu et al. [8] showed that the epithelial-to-mensenchymal transition leading to

cancer metastasis are linked to changes in mechanical characteristics of the cytoskeleton influencing the vimentin network [7, 8] as well as the polarity of the cell [9]. Moreover, cancer cells are typically found to be softer than normal cells. A decrease in the level of actin in the cytoskeleton of cancerous cells was linked to changes in the mechanical properties of the cell [10]. Such research underpins the importance of linking molecular changes within the cytoskeleton to structural and functional changes of the entire cell and therefore changes to the tissue.

In summary, in-depth knowledge of cellular and sub-cellular mechanics might allow the identification and classification of cells at different physiological and patho-physiological stages. However, to do so, new methods and approaches need to be developped that are capable of simultaneously performing structural and mechanical analysis of sub-cellular structures in a (semi-)automated way. Such methods do not exist. Therefore, the link between the mechanical stability and its contribution to shaping processes on the molecular scale are far from being completely understood. Further, it is not clear, if mechanical processes, besides conveying biochemical signals, also purely convey mechanical signals to invoke structural changes. The concept of the cytoskeleton as a shape-determining scaffold for the cell is well established [11], however, the tight coupling of actin, microtubule and intermediate filament networks impedes a separate analysis. To date, computer models of cytoskeletal biopolymer networks are based on models that represent the geometry in a (strongly) simplified way, see, for example, [12–16]. In depth analysis of structure-function relationships, however, require detailed structural and functional modelling.

Development of such models requires a protein network with similar structural functionality to cytoskeletal networks while being structurally less complicated allowing a semi-manual validation of the derived results. Proteins homologous to tubulin, which is part of the eukaryote cytoskeleton, such as the Filamentous Temperature Sensitive Z (FtsZ) protein family in the chloroplasts of the moss *Physcomitrella patens* are excellent examples for this purpose. They generate complex polymer networks, showing striking similarity to the cytoskeleton, and hence were named plastoskeleton [17]. In bacteria, FtsZ is a part of the bacterial cytoskeleton providing a scaffold for cell division [18–20]. Coassembly experiments provide evidence that FtsZ2 controls filament morphology and FtsZ1 promotes protofilament turnover. It is suggested, that *in vivo*, FtsZ2 forms the chloroplast Z-ring backbone while FtsZ1 facilitates Z-ring remodeling [21]. Moreover, as chloroplasts in loss-of-function mutants show distinct shape defects, FtsZ networks might provide scaffolds that ensure the stability and structural integrity of the chloroplasts [22]. Additionally, gene knock-out experiments has shown that the FtsZ network is capable of undergoing large deformations upholding its structural integrity [23]. This adaptive stability is presumably linked to the developed structural characteristics of FtsZ network; making the cytoskeletal FtsZ network an ideal first application for introducing and testing a simulation-based method that aims to identify the link between structural features of a cytoskeletal network and its mechanical functions.

State-of-the-art microscopy imaging techniques permit resolving micro-structural details of protein networks. Computational analysis of acquired images facilitates the quantification of components and its assembly to networks [24], and may allow tracking structural changes

of the network assembly triggered by internal or external stimuli, i.e., connecting the structure to functionality or distinguishing between network types [25]. Machine learning (ML) algorithms have proven to be remarkably capable for automating such complex image analysis tasks [26] and of correlating image content to biological structural functionality [27–29]. Recently the concept of ML-based surrogate models has proven to be highly advantageous in accelerating the performance of numerical simulations of complex mechanical environments [30] as well as predicting material properties [31]. A ML-based approach could link structural features to mechanical characteristics and would provide a way to answer questions like those posed in the abstract, e.g. "How are FtsZ biopolymers capable of exhibiting adaptive stability?" or "Interplay of which structural changes in the cytoskeleton of a cancerous cell leads to adapting stiffness?"

To overcome the challenge of relating structure to function of cytoskeletal protein networks, we present an automated ML approach applied to 3D live laser scanning confocal microscopy images. The outcome is an end-to-end tool that links structural features associated with the cytoskeletal network type to its mechanical behaviour and therefore enables an online evaluation of structure-function relations on the sub-cellular scale. This is carried out by combining an in silico mechanical characterization of protein networks through 3D micro finite element modeling and an automatic mapping of structural features to the mechanical network responses. The introduced method (1) classifies protein networks based on their structural features exploiting a random forest model and (2) creates an in silico surrogate model to predict the sub-cellular mechanical responses of the network. Analyzing the prediction process of the surrogate model based on the structural feature allows us to deduct the presumed structure-function relationship. The method is tested and applied to elucidate isoform-specific structure-function relationships of FtsZ networks. While the two FtsZ isoforms, FtsZ1-2 and FtsZ2-1, were selected in this work as a first application to perform a proof-of-concept study, future applications will address more complex networks.

2. Materials and Methods

2.1. Materials

The “Gransden 2004” ecotype of the moss *Physcomitrella patens* ((Hedw.) Bruch & Schimp., IMSC accession number 40001) was cultivated in bioreactors [32].

2.2. Molecular Biology and Moss Transfection

RNA isolation, molecular cloning and moss transfection were described previously in detail [24, 25] and are therefore given here only in a shortened version. Total RNA was isolated from wild type *Physcomitrella patens* protonema using TRIzol Reagent (Thermo Fisher Scientific) and used for cDNA synthesis using Superscript III reverse transcriptase (Life Technologies, Carlsbad, CA, USA). The coding sequences of PpFtsZ1-2 and PpFtsZ2-1 were PCR-amplified from this cDNA and cloned into the reporter plasmid pAct5::Linker:EGFP-MAV4 (modified from [33]) to generate the fusion constructs PpAct5::PpFtsZ1-2::linker::EGFP-MAV4 and PpAct5::PpFtsZ2-1::linker::EGFP-MAV4. Moss protoplasts were isolated and transfected with $50\,\mu g$ of each of these plasmids, according to the protocol described by

Hohe et al. [34]. The transfected protoplasts were incubated for 24 h in the dark, subsequently being returned to normal conditions ($25.1°C$; light-dark regime of $16:8h$ light flux of $55\,\mu mol\,s^{-1}m^{-2}$ from fluorescent tubes, Philips TL - 19 - 65W/25).

2.3. Laser Scanning Confocal Microscopy Imaging

In $4-7$ days after transfection, the protoplasts were concentrated to a volume of $100\,\mu l$, and $20\,\mu l$ of this protoplast suspension was used for imaging. Confocal microscopy images ($n = 37$, i.e., 21 FtsZ2-1 and 16 FtsZ1-2 isoforms) were taken with a Leica TCS SP8 microscope (Leica Microsystems, Wetzlar, Germany), using the HCX PL APO 100x/1.40 oil objective and applying the microscopy conditions described previously [24, 25]. A selection of images visualising FtsZ networks is depicted in Fig. 1a. To summarise, the zoom factor was 10.6, the voxel sizes were $0.021\,\mu m$ in the $X-Y$ dimensions and $0.240\,\mu m$ in the Z dimension and the pinhole was adjusted to $0.70AU$ ($66.8\,\mu m$). For the excitation, a WLL laser was applied at $488\,nm$ with an intensity of 4%. The detection ranges were set to $503-552\,nm$ for the EGFP fluorescence and $664-725\,nm$ for the chlorophyll autofluorescence. All images were deconvolved using Huygens Professional version 17.04 (Scientific Volume Imaging, The Netherlands).

2.4. Image Processing to Extract Structural Features

A set of 26 structural features describing the assembly of protein networks from global and local perspectives is extracted from each network. Here, only a short description of the workflow steps and features are given, details as well as a validation have been reported previously [24].

2.4.1. Image Pre-processing

Networks are extracted from the images using an adaptive local threshold, $T = m + k\sqrt{\frac{1}{NP}\sum_{i=1}^{NP}(p_i - m)^2}$, with $NP = 10*10*10$ being the local window size, m is the average pixel intensity in the window, p_i denotes the intensity of pixel i and a constant value $k = 10$. Next, by calculating the convex hull of the segmented network a solid outer surface representing the volume enclosing the network is determined. To extract the structural features of the network, a transformation to a spatial graph consisting of points, nodes and segments is performed. This transformation consists of following steps: 1. determining the centerline of each filament based on calculating a distance map for each foreground voxel from the edge voxels, and 2. placing points at the centerline of the filaments where either thickness or the direction of the filament changes. The resulted hierarchy of structural elements of the spatial graph reads as: 1. points, 2. elements as the connection between points, 3. nodes, as points that are connected to more than two other points, 4. segments as summation of elements from one node to another (filaments), 5. connections as the meeting points of filaments in a node. This resulting numerical representative in form of a spatial graph allows determination of structural features (Fig. 1b).

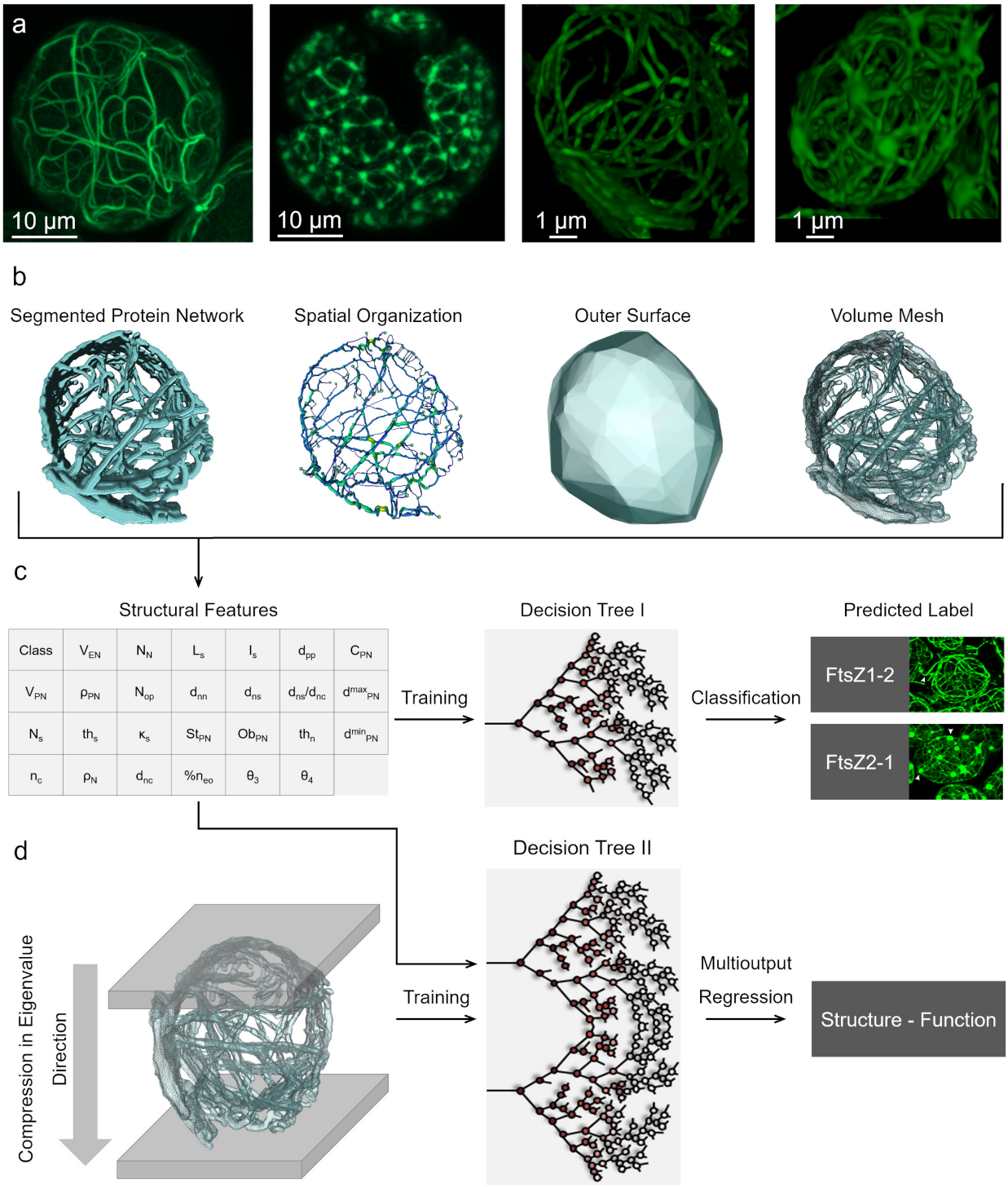

Figure 1: End-to-end prediction of FtsZ mechanical behavior from CLSM images. a) Sample 3D CLSM images of FtsZ1-2 and FtsZ2-1 networks in a cell (two left images) and single FtsZ1-2 and 2-1 networks (two right images), respectively. b) Sample of a 3D segmented image and its spatial graph, convex hull and mesh. c) The 26 shape and element descriptors that are extracted and used as input features to train a random forest model for classifying FtsZ1-2 and FtsZ2-1 isoforms. d) A second random forest model (multi output regression) is trained on the structural features to predict the results of the mechanical simulation of compressing the network in its principal directions (3 Eigenvectors).

2.4.2. Features Describing 3D Network Morphology

A set of seven shape descriptors, which were determined from a simultaneous analysis of the segmented network, and its convex hull quantitatively describe the morphology of the network [24]. These features consist of: 1. enclosed volume of the network, V_{EN}, as the volume of the convex hull, 2. network volume, V_{PN}, as the volume of the segmented protein network, and 3. the network volume density, ρ_{PN}, as the ratio of enclosed volume to network volume. Furthermore, a shape matrix representing the covariance of the convex hull is calculated. Building upon the eigenvalues of the shape matrix, the 4. greatest and 5. smallest diameters of the network, d_{PN}^{max} and d_{PN}^{min}. 6. stretch of the network, St_{PN}, and 7. oblateness of the network, Ob_{PN} are determined.

2.4.3. Features Describing Network Structure

A set of 19 local structural features calculated from the spatial graph of the network consists of nodal features (1. number of nodes, N_n, 2. thickness of nodes, th_n, 3. node density, ρ_n, 4. node-to-node distance, d_{nn}, 6. node-to-surface distance, d_{ns}, 6. node-to-centre distance, d_{nc}, 7. number of open nodes, N_{op}. 8. compactness, C_{PN}, defined as $C_{PN} = (d_{nc} - d_{ns})/d_{nc}$. 9. node-to-surface to node-to-center ratio), segment features (10. number of segments, N_s, 11. segment length, L_s, 12. segment curvature, κ_s, 13. mean segment thickness, th_s, 14. segment inhomogeneity, I_s, 15. segment point-to-point distance, d_{pp}), and connection feature (16. mean number of connections per node, n_c 17. percentage of open nodes, n_{oe}, 18./19. mean angles between segments in a connection with 3/4 filaments meeting, θ_3 and θ_4). The morphological and structural features are calculated by a set of in-house Matlab codes (Matlab 2019a, MathWorks, USA).

2.5. Mechanical nano-FE modeling

To investigate the mechanical response of the protein networks to external load, we designed a generic in-silico experiment reflecting a compression against a plate, hence, a scenario that is typically also used to experimentally investigate the mechanical behaviour of whole cells [35]. To capture the overall mechanical behavior of each network in a comparative manner, compression tests along the three principal axis of each system were modeled employing a nano-FE approach. All simulations were done with the finite element analysis software Abaqus 6.14 (Dassault Systèmes, France). It is important to note that, the goal of this setup is to depict the mechanical behavior of the protein network morphology rather than replicating the real physical condition and dynamics of the biopolymers in their biological roles. Such a task would require consideration of highly complicated interactions of the network with its surrounding, which are not completely understood to date.

2.5.1. 3D Protein Network Model Generation

For all samples, protein network surface meshes were defined from the segmented images using a triangular approximation algorithm coupled with a best isotropic vertex placement algorithm to achieve high triangulation quality [36]. The surface area of the resulting surface mesh was calculated and further remeshed using $n_t = \rho_t A_t$ triangles for the remeshed surface, where $\rho_t = 900\,[triangles/\mu m^2]$ is the constant surface mesh density and A_t denotes

the surface area. Furthermore, the remeshed surface was smoothed by shifting the vertices towards the average position of its neighbours. The enclosed surfaces were filled with volumetric tetrahedral elements, resulting in an adaptive multi-resolution grid (Fig. 1b) using FEI Amira 6.3.0 (Thermo Fisher Scientific, USA).

The principal directions of a network were determined based on its convex hull and shape matrix. The eigenvectors of the shape matrix ($EV1$, $EV2$ and $EV3$), which are orthogonal to each other, represent the network's principal directions, V_i ($i = 1, 2, 3$). The mesh is then transformed to the coordinate system spanned by V_i. Afterwards, along each V_i, the pair of nodes exhibiting the largest distance in-between the two points and in the direction of V_i were determined and named N_{i1} and N_{i2} and $i = 1, 2, 3$, respectively.

For each considered protein network, the geometry of the protein network was imported to Abaqus 6.14 (Dassault Systèmes, France). For each network, three compression simulations (one per direction d) were carried out. For each simulation, the initial set-up was determined by first identifying the initial position of two parallel rigid plates, which are defined for each simulation in direction d by its normal vector $\overrightarrow{N_{d1}\,N_{d2}}$ (with $d = 1, 2$, or 3), and the respective nodal points N_{d1} and N_{d2} (cf. Fig. 2a, 2b, and 2c).

2.5.2. Governing equations

The simulations were carried out by solving the balance of linear momentum in an explicit manner (Eq. 1),

$$\rho\dot{\mathbf{v}} - \nabla \cdot \boldsymbol{\sigma} - \rho\mathbf{b} = \mathbf{0}, \tag{1}$$

where ρ is the mass density, $\mathbf{v}$ denotes the velocity, $\boldsymbol{\sigma}$ describes the Cauchy stress, and $\mathbf{b}$ are the body forces. The contact between the protein network and the rigid plates was chosen as a rough contact meaning that any two points, which come in contact, will stick together with a relative penetration tolerance of 1 e−3. The governing equation is discretised using the FE method and choosing tetrahedral elements and linear spatial Ansatz functions.

2.5.3. Boundary Conditions

The generic boundary conditions for each simulation setup (one simulation for each primary directions: $EV1$, $EV2$ and $EV3$) consist of applying displacement boundary conditions at node N_{d1} to mimic compression experiments. The displacement itself is applied in the $EV_d = \overrightarrow{N_{d1}\,N_{d2}}$ direction and in fractions (α) of the initial distance, $\|\overrightarrow{N_{d1}\,N_{d2}}\|$, between the two plates (cf. Fig. 2). Therefore, the amount of displacement along the respective Eigenvector EV_1 is defined by $U_d = \alpha \cdot \|\overrightarrow{N_{d1}\,N_{d2}}\|$.

To investigate anisotropy in the mechanical response of the network, compression tests along all three primary directions were performed and compared. Furthermore, for analyzing changes in the structural behavior with increasing deformation grade, we increased the displacement of the plate gradually in steps of $\delta\alpha = 0.02$. We applied a total of 10 steps, which is equivalent to $\alpha = 0.20$. Due to no apparent significant differences in the mechanical behaviour of the network between the three directions at $\alpha = 0.20$ and the required computational resources, we chose to focus only on one direction to continue the simulations for $\alpha = 0.02 \rightarrow 0.20$.

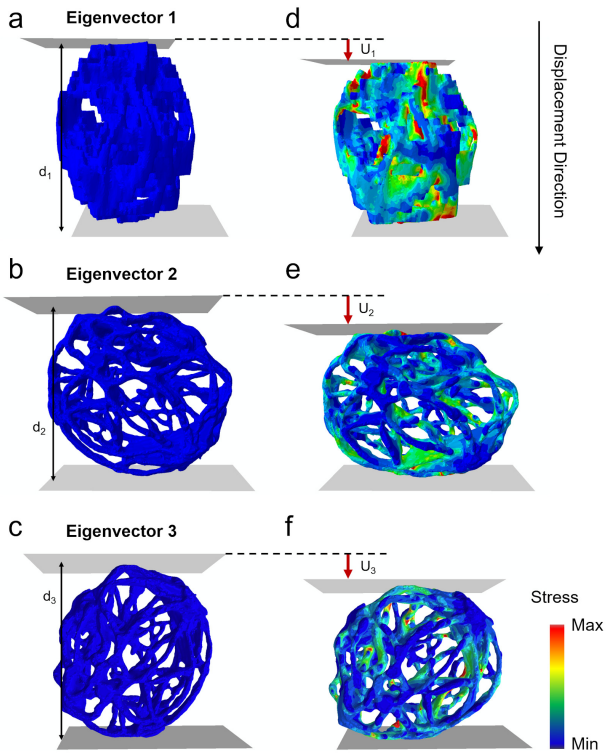

Figure 2: Simulation setups. a-c) Initial set-up for virtual compression experiments of a sample protein network in primary directions EV1, EV2 and EV3, respectively. d-f) Stress distribution after applying a displacement ($\alpha = 0.02$) to the upper plate in EV1, EV2 and EV3 directions, respectively. The displacements are scaled by a factor of 5.

2.5.4. Constitutive Law and Material Parameters

Employing the concept of linear elasticity, the stress tensor $\boldsymbol{\sigma}$ is given by

$$\boldsymbol{\sigma} = \lambda \, \mathrm{tr}(\boldsymbol{\epsilon}) \, \mathbf{I} + 2\mu\boldsymbol{\epsilon}, \tag{2}$$

where $\boldsymbol{\epsilon}$ denotes the strain tensor and $\boldsymbol{I}$ is the second-order identity tensor. Further, λ and μ are the first and the second Lamé coefficients, respectively. The Lamé coefficients are related to Young's modulus E and Poisson's ratio ν by

$$\lambda = \frac{E\nu}{(1+\nu)(1-2\nu)}, \quad \mu = \frac{E}{2(1+\nu)}. \tag{3}$$

In clasical continuum mechanics, the material parameters (here λ and μ or E and ν) are obtained by making a constitutive assumption, i.e., selecting a particular phenomenological constitutive law (here the form of $\boldsymbol{\sigma}$) and ensuring that the computed stresses match the experimental ones. The mechanical behavior of filamentous biopolymers is, however, commonly quantified by means of the flexural rigidity, κ [37–39], which is the force couple required for one unit of curvature [40]. The flexural rigidity, κ, is defined as $\kappa = EI$, where

I is the second moment of inertia. In the context of protein filament mechanics, the flexural rigidity is calculated as $\kappa = k_B T l_p$, where $k_B = 1.38 \cdot 10^{-23}$ J/K is the Boltzmann constant, T defines the temperature, and l_p denotes the corresponding thermal persistence length. For the persistence length of FtsZ filaments, there exist multiple atomic force microscopy studies [41–44]. Turner et al. report, for example, for the persistence length and flexural rigidity of FtsZ filaments $\kappa = 4.7 \pm 1.0 \times 10^{-27}\,\mathrm{Nm}^2$ and $l_p = 1.15 \pm 0.25\,\mu\mathrm{m}$ [45], respectively. These values have also been commonly used in other research, see, e.g., [46]. The average thickness of filamentous elements of the FtsZ network is $117 \pm 28\,\mathrm{nm}$ [25]. Assuming circular cross sections, I equals $1.81 \times 10^{-29}\,\mathrm{m}^4$ [47]. Based on these values, we set within our simulations the elasticity modulus to $E = 2.6 \times 10^2\,\mathrm{Pa}$ and the Poisson's ratio to $\nu = 0.5$, i.e., assume incompressibility [46, 48, 49].

2.5.5. Calculated Mechanical Parameters

We performed a total of 111 simulations (3 simulations per network) on a CPU cluster with 32 cores (4 AMD Opteron Socket G34 Eight-Core 6328, 3.2 GHz, 8C, Abu Dhabi). One simulation took on average 19 ± 7 hours (for the entire 20% compression). To quantitatively assess the mechanical behavior of the protein networks, we determined the mean stress and strain of the networks, $\bar{\sigma}$ and $\bar{\epsilon}$, respectively, as the average of the L1 norms of the von Mises stresses and principal strains.

Cytoskeletal structures are reported to fail by buckling or rupture [50]. We therefore, further analyzed the structural stability of the network by calculating a buckling failure factor based on critical stresses σ_{crit} and a rupture failure factor based on critical strains ϵ_{crit}. Buckling of a single filament is assumed to happen if local von Mises stresses exceed a critical value. A filament is assumed to rupture, if strains locally exceed a critical strain value. To our knowledge, data for σ_{crit} and ϵ_{crit} do not exist for FtsZ in the literature. However, despite fundamental structural differences, F-actin and FtsZ show similar mechanical behavior. The rigidity of F-actin is assumed to be $\kappa = 7.5 \cdot 10^{-26}\,\mathrm{Nm}^2$ [37, 51] whereas the rigidity, which we assume for FtsZ filaments, is $\kappa = 4.7 \pm 1.0 \times 10^{-27}\,\mathrm{Nm}^2$ (l_p of F-actin: $1.77\,\mu m$ and l_p of FtsZ: $1.15\,\mu m$ [37, 45]). Therefore, we use the values reported for F-actin ($\sigma_{crit} = 3.2\,Pa$ and $\epsilon_{crit} = 0.2$ [49, 51]). Since a local failure might not lead to a collapse of the whole network structure, we define failure factors based on the assumption that if a certain portion m of all elements ($m \cdot n_{all}^{elem}$) exhibit stresses or strains above the critical stress or strain value, the whole structure will fail by buckling or rupture of an individual or several segments, This assumption has also been made for other biological materials [35, 52]. For protein networks, these threshold values have not been experimentally investigated yet. Therefore, we report only the portion of elements that exceed a particular critical stress or strain value, i.e., the higher the values the higher the failure probability. We define the buckling failure factor as $FB = n_{\sigma_{crit}}^{elem} / n_{all}^{elem}$, and the rupture failure factor as $FR = n_{\epsilon_{crit}}^{elem} / n_{all}^{elem}$, where n_{all}^{elem} is the total number of elements, $n_{\sigma_{crit}}^{elem}$ and $n_{\epsilon_{crit}}^{elem}$ are the number of elements with stress and strain exceeding the critical buckling or rapture values, respectively.

2.6. Data-driven Analysis using Machine Learning

To relate the mechanical functionality of protein networks to their structure, we utilize a ML approach. This allows us to 1) find the characteristics that distinguishes two FtsZ isoforms, and 2) extract structural features correlated to the mechanical behavior of the networks. Analyzing the extracted features empowers us to identify design approaches developed by nature for carrying out mechanical functionality. To do so, we trained two sets of ML models on the 26 calculated structural features of the protein networks. The aim of these ML models is to 1) perform an end-to-end classification of the networks as well as an analysis of the structural features dominating the decision process and 2) map the structural features of the network to its mechanical behavior by employing a regression model. This further allows us to identify the most dominant structural features contributing to specific mechanical traits of the network.

2.6.1. Classification of FtsZ Isoforms

We employed a random forest model to perform the classification task based on the extracted features (Fig. 1c), which is the state-of-the-art method for classification based on a set of unstructured features [53, 54]. The dataset containing the 26 structural features was randomly divided eight times into training ($n = 30$) and testing ($n = 7$) sets. Due to the strong law of large numbers guaranteeing the absence of over-fitting [55], no validation set is needed. Each testing sets consisted of at least three samples of each isoform. For each data division, a random forest classification model was built upon the extracted structural features with the isoform (FtsZ1-2 or FtsZ2-1) as output class. This allows refuting dependency of the classification results on the train/test dataset division. The Gini index was used as attribute selection measure [53, 56]:

$$G_{C_i} = \sum \sum_{j \neq i} (f(C_i, T)/|T|)(f(C_j, T)/|T|), \tag{4}$$

with $(f(C_i, T)/|T|)$ determining the probability of the selected cases belonging to the class C_i (FtsZ1-2 or FtsZ2-1) for the given training set T.

2.6.2. Surrogate Mechanical Model for Predicting Function from Structure

To investigate the structural approach(es) employed by nature to provide networks with specific mechanical functionality, i.e., adaptive stability, a set of surrogate models is designed. The surrogate models serve as a tool to map the structural features of the protein networks to their mechanical behavior. First, four multi-output-regression-random-forest models, as introduced by Breiman et al. [54] were trained by forming trees mapping the 26 structural feature on the calculated mechanical parameters ($\bar{\sigma}, \bar{\epsilon}, FB$ and FR, cf. 2.5.5). This is done for all three primary directions ($EV1$, $EV2$ and $EV3$) and 2% compression (Fig. 1d). Second, based on the simulation results for compressing the protein network by 20% in the EV3-direction, we trained a set of single-output-regression-random-forest models for each of the calculated mechanical parameters ($\bar{\sigma}, \bar{\epsilon}, FB$ and FR; four models per mechanical parameter). For each ML model, a random dataset division with 32 and 5 networks

was carried out for training and testing purposes (enforcing that at least 2 networks from each isoforms were considered). All random forest algorithms were implemented using the machine learning library Scikit-learn in Python 3.7 [57].

2.6.3. Analyzing Feature Importance

We determined the importance of each structural feature in both the classifier and the surrogate mechanical models. To do so, each feature is noised up and the plurality of out-of-bag vote and the reality are determined allowing to measure a wrong prediction rate [54] for each feature.

2.6.4. Statistical Analysis

To distinguish the mechanical behavior of FtsZ1-2 isoforms from FtsZ2-1 isoforms, statistical analysis of $\bar{\sigma}$, $\bar{\epsilon}$, FB and FR was performed using repeated measures ANOVA and paired or unpaired student's t-tests, as appropriate, followed by Bonferroni corrections for multiple comparisons. All values are presented as mean $\pm$ standard deviation and statistical significance was set to $p < 0.05$.

2.7. Assessing Machine Learning Model Performance

The performance of the classifier model is evaluated by calculating the $F1$-score and the area under the receiver operating characteristic (ROC) curve [58]. The performance of each surrogate model is assessed by calculating R^2-values between the model predictions and simulation results. To further measure the differences between the surrogate model predictions and the true values of simulation results, we calculated the coefficient of determination (R^2_E) of the linear fit for scattered data of model predictions vs. simulation results. In addition, we define $E_a = |1 - a_{SM}|$ as the difference of first derivative of the linear fit to one, with $E_a = 0$ denoting a perfect surrogate model.

3. Results

3.1. Effect of Load Direction on Mechanical Response

$N = 16$ FtsZ1-2 and $n = 21$ FtsZ2-1 isoforms images (see examples in Figure 3a, e) were processed. For each protein network, the image processing resulted in distinct spatial graphs (Fig. 3b, f), convex hulls (Fig. 3c, g), and FE meshes (Fig. 3d, h).

All mechanical parameters ($\bar{\sigma}$, $\bar{\epsilon}$, FR and FB) were affected by load direction as well as isoform type (ANOVA, $p < 0.01$). $\bar{\sigma}$, in the FtsZ1-2 isoform, was significantly lower for the EV2 load case than for the other two load cases ($p = 0.01$, Fig. 4a). For the FtsZ2-1 bucking failure (FR) was significantly lower for EV1 load case if compared to the EV3 load casa ($p < 0.01$, Fig 4d). Comparing the mechanical parameters (x, $\bar{\epsilon}$, FR, FB) between the isoforms revealed that all mechanical parameters of the FtsZ2-1 isoform were for the EV2 loading case significantly higher than for the FtsZ1-2 isoform ($p \leq 0.04$; Fig. 4a-d). Additionally, FtsZ2-1 responded to compression in EV3 direction with a significant higher $\bar{\epsilon}$ than FtsZ1-2 ($p = 0.049$; Fig. 4b).

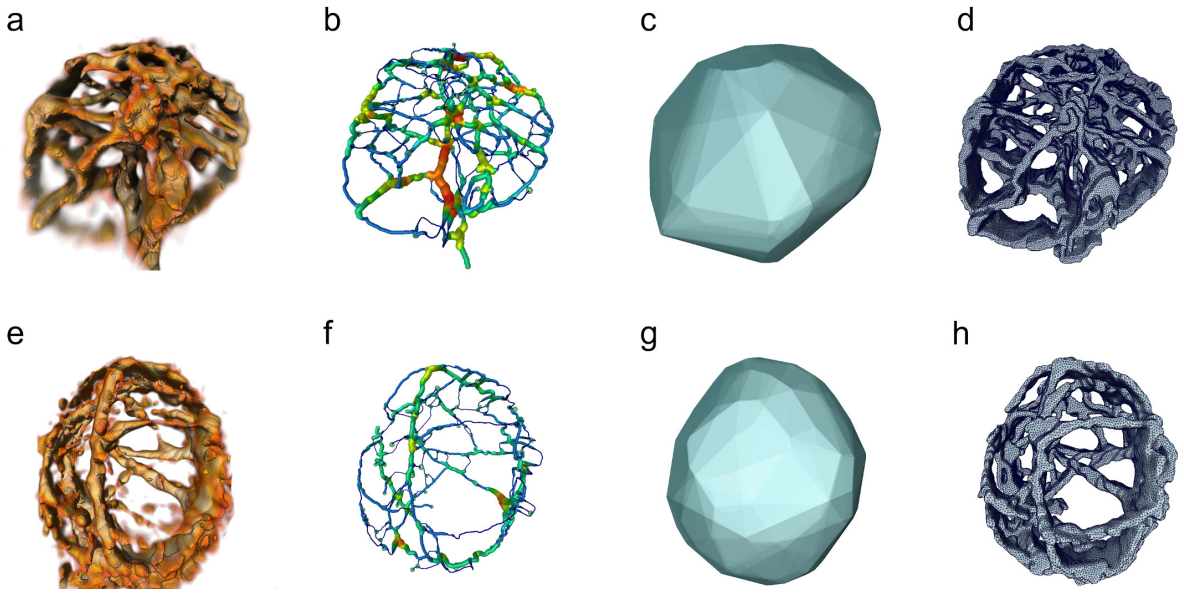

Figure 3: Image pre-processing of FtsZ1-2 (a-d) and FtsZ2-1 (e-h) isoforms. a) Sample 3D CLSM image of FtsZ1-2 isoform, b) resulting spatial graph, c) resulting convex hull and d) resulting volume mesh. e) Sample 3D CLSM image of FtsZ2-1 isoform, f) resulting spatial graph, g) resulting convex hull and h) resulting volume mesh.

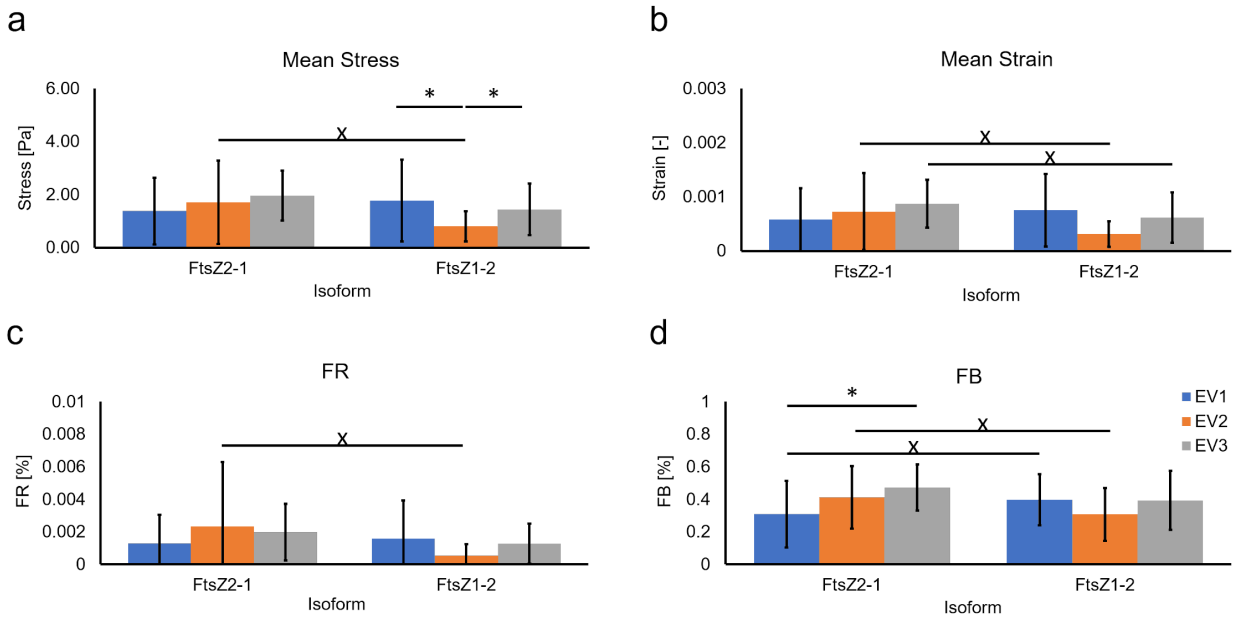

Figure 4: Mechanical responses to small deformations (2% compression). a) $\bar{\sigma}$. b) $\bar{\epsilon}$. c) FR d). FB. Data is shown as mean±standard deviation. * denotes a significant difference between load directions (student's t-test, Bonferroni correction), X denotes a significant difference between isoforms. Data is shown as mean±standard deviation.

3.2. Effect of displacement on mechanical response

Here we focus only on one direction due to four reasons: 1) the similar mechanical response at 2% displacement for all loading cases, 2) according to calculations in [24], variations of the two significant different parameters for all three principal directions (FtsZ1-2: $\bar{\sigma} = 55\%$ and FtsZ2-1: $FB = 35\%$) can be explained by differences in stretch (FtsZ1-2 $St = 0.76 \pm 0.11$, FtsZ1-2 $St = 0.67 \pm 0.20$, $p = 0.05$), 3) the need of significant computational resources and 4) EV3 has the overall highest (combining FtsZ2-1 and FtsZ1-2) mean values at 2% plate displacement in all four parameters ($\bar{\sigma} = 1.7 \pm 1.3\,Pa$; $\bar{\epsilon} = 0.7 \pm 0.6\,\mathrm{e}{-3}$; $FR = 1.6 \pm 3\,\mathrm{e}{-3}$; $FB = 4.2 \pm 1.9\,\mathrm{e}{-1}$). Therefore, we decided to restrict ourselves to investigating the mechanical response of the system for only EV3 principal direction.

Increasing the compression of the isoforms from 2% to 20% (Fig. 5)revealed that, at all displacement steps, no significant difference between the two isoforms in the four calculated mechanical parameters exists (Fig. 5c-f). For mean stress, mean strain and rupture failure factor (Fig. 5c-e), a gradual increase in both network types was detected with increasing displacements. In contrast, with increasing compression, FB converges toward a buckling failure factor of 1% (Fig. 5f).

Comparing the mechanical responses at 20% displacement shows no significant difference between the two FtsZ isoforms (Fig. 5h). At 20% displacement, the buckling failure factor (FtsZ1-2: 1.0% and FtsZ2-1: $1.0 \pm 0.1\%$) is significantly higher than the rapture failure factor (FtsZ1-2: $0.4 \pm 0.2\%$ and FtsZ2-1: $0.5 \pm 0.2\%$, $p \leq 0.01$). However, the first derivative of the failure factors with respect to the displacement (FR: FtsZ1-2: 0.02, FtsZ2-1: 0.03 and FB: FtsZ1: 0.00, FtsZ2-1: 0.00) shows that with increasing displacement, FR would presumably become the dominating failure factor.

3.3. End-to-end Isoform Classification based on Structural Features

All of the 8 classifier models trined on the 26 structural features (cf. 2.6.1) reached 6 out of 7 correct predictions (Fig. 6a). The classifier models reached an average $F1$-score of 0.83 ± 0.11 and an area under the ROC curve of 0.86 ± 0.08 (Fig. 6b). A correctly classified FtsZ2-1 isoform and a correctly classified FtsZ1-2 isoform, as well as the wrongly classified isoform (FtsZ1-2) are depicted in Fig. 6c-e, respectively. . The classification took on average $5.1\,s$.

Analyzing the importance of each of the structural features in the classification models reveals which of the features contribute most and which least in terms of classifying isoform-inherent structural properties. The five most important structural features are the percentage of open ends ($19 \pm 5\%$, $p < 0.01$), segment curvature ($12 \pm 9\%$, $p = 0.05$), network volume density ($8 \pm 4\%$, $p = 0.03$), compactness ($6 \pm 3\%$, $p = 0.24$), and the mean segment thickness ($5 \pm 7\%$, $p = 0.01$). These have in total 50% of the overall importance in the classification models (Fig. 7). Interestingly, the number of open ends and the smallest network diameter were significantly different between the two isoforms, but of less importance for its classification.

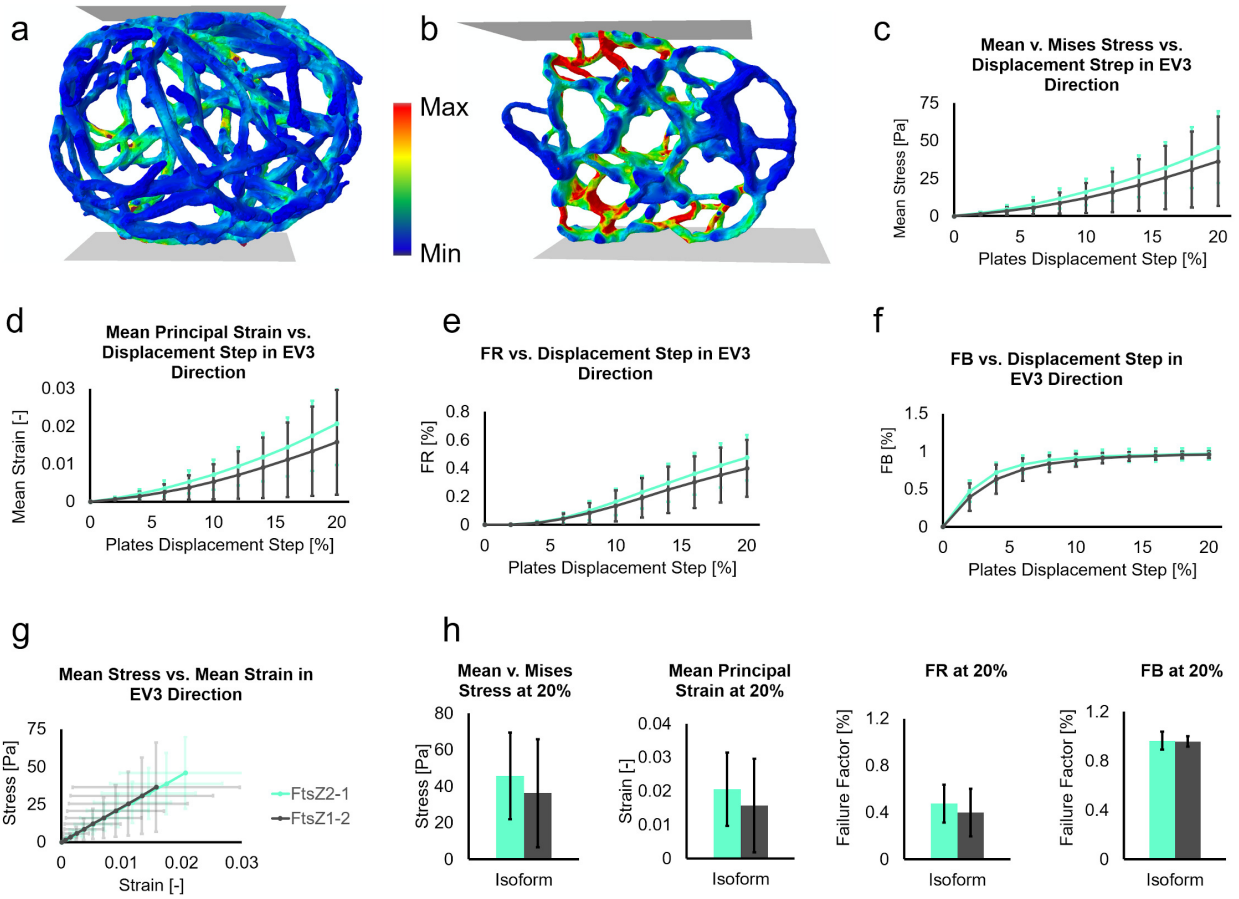

Figure 5: Changes in mechanical response with increasing compression. a, b) Stress distributions at 20% displacement in sample networks of FtsZ1-2 an FtsZ2-1, respectively. c) $\bar{\sigma}_{EV3}$. d) $\bar{\epsilon}_{EV3}$. e) FR_{EV3}. f) FB_{EV3}. g) Mean stress vs mean strain in EV3 direction. h) Calculated mechanical parameters ($\bar{\sigma}_{EV3}$, $\bar{\epsilon}_{EV3}$, FR_{EV3} and FB_{EV3} respectively) at the 20% displacement step. Results are presented as mean±standard deviations. * denotes a significant difference based on student's t-test ($p < 0.05$) between FtsZ1-2 (gray) and FtsZ2-1 (green). Displacement step size 2%, minimum displacement 2%, maximum displacement 20%.

3.4. End-to-end Mechanical behavior Prediction based on Structural Features

The trained surrogate model predicted the mechanical response (simulation results) for small (2%) and large (20%) deformations purely based on structural features with high correlations between simulated and predicted mechanical parameters. In case of small deformations, the predictive models show high accuracy for predicting stresses, $\bar{\sigma}$ ($R^2 = 0.90$, $E_a = 0.03$ and $R^2_E = 0.83$; Fig. 8a) and strains, $\bar{\epsilon}$ ($R^2 = 0.81$, $E_a = 0.04$ and $R^2_E = 0.45$; Fig. 8b). However, for predicting failure due to rupture FR ($R^2 = 0.69$, $E_a = 0.04$ and $R^2_E = 0.69$; Fig. 8c) and buckling FB ($R^2 = 0.72$, $E_a = 0.06$ and $R^2_E = 0.60$; Fig. 8d) the surrogates' model to predict these mechanical parameters are slightly lower. In case of large deformations, however, all four mechanical parameters are predicted with high accuracy. The best performing of the 4 trained surrogate models shows great prediction metrics for $\bar{\sigma}$

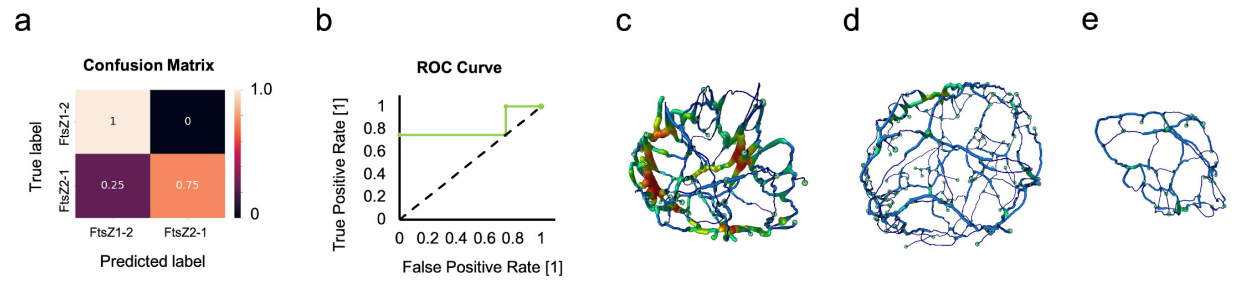

Figure 6: End-to-end classification of isoforms. a) Confusion matrix of prediction performance with 3 out of 3 correct predictions for FtsZ1-2 and 3 out of 4 correct predictions for FtsZ2-1. b) ROC curve of model prediction. c) A sample spatial graph of correctly classified FtsZ2-1. d) A sample spatial graph of correctly classified FtsZ1-2. e) A sample spatial graph of wrongly classified FtsZ1-2.

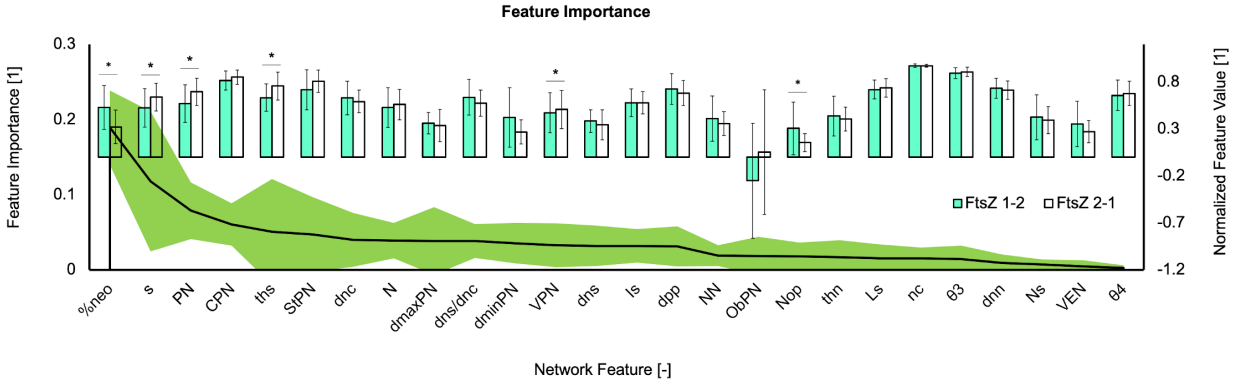

Figure 7: Mean classification importance for the structural features as well as normalized feature values (normalized to maximum of each feature). Data shown as mean ± standard deviation. * indicates a significant difference between isoform (un-paired students' t-test).

($R^2 = 0.99$, $E_a = 0.03$ and $R^2_E = 0.98$; Fig. 8e), $\bar{\epsilon}$ ($R^2 = 0.98$, $E_a = 0.01$ and $R^2_E = 0.98$; Fig. 8f), FR ($R^2 = 0.97$, $E_a = 0.01$ and $R^2_E = 0.95$; Fig. 8g) and FB ($R^2 = 0.99$, $E_a = 0$ and $R^2_E = 0.98$; Fig. 8h).

The analyzed structural features have different importance in predicting the mechanical parameters in case of large deformations. For predicting the mean stresses, most important features (50% of total importance) are segment inhomogeneity (I_S: 17±5%), network density (ρ_{PN}: $16 \pm 9\%$), segment thickness (th_S: $9 \pm 3\%$) and number of open nodes (N_{op}: $8 \pm 2\%$; Fig. 8i). In case of predicting the mean strains, segment inhomogeneity (I_S: $37 \pm 18\%$), number of open nodes (N_{op}: $12 \pm 17\%$), network density (ρ_{PN}: $8 \pm 12\%$) and oblateness of the network (Ob_{PN}: $6 \pm 10\%$) were the most important structural feature (Fig. 8j). The prevailing structural features for predicting the rapture failure factor are network density (ρ_{PN}: $18 \pm 8\%$), segment inhomogeneity (I_S: $13 \pm 9\%$), node density (ρ_N: $9 \pm 3\%$) and segment thickness (th_S: $8 \pm 12\%$; Fig. 8k). In case of predicting the buckling failure factor, node-node distance (d_{nn}: $34 \pm 20\%$), segment inhomogeneity (I_S: $22 \pm 12\%$), point-point distance (d_{pp}: 8±8%) and number of segments (N_S: 5±7%) are the most important features

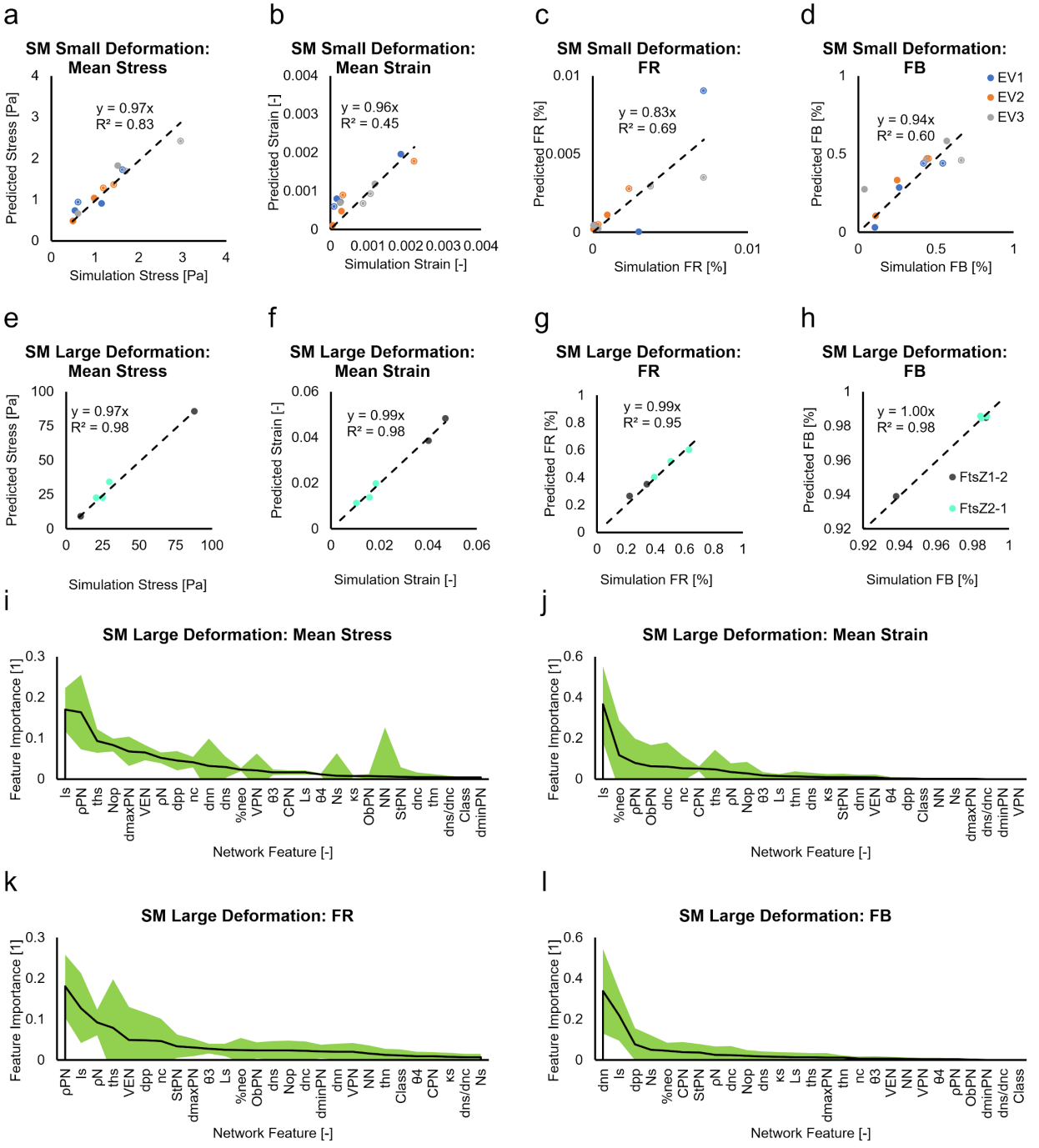

Figure 8: Surrogate mechanical model. a-d) Surrogate model prediction vs. simulation results for the test set networks for small deformation in each primary direction (EV1: blue, EV2: orange and EV3: gray. a) $\bar{\sigma}$. b) $\bar{\epsilon}$. c) FR. d) FB. Networks of FtsZ1-2 in the test set are shown as solid circles and FtsZ2-1 as circles with an outer ring. Dashed line represents a liner fit to the data points. e-h) Surrogate model prediction vs. simulation of best performing model results for the test set networks for large deformation in EV3 direction. e) $\bar{\sigma}$. f) $\bar{\epsilon}$. g) FR. h) FB. Gray and green circle represent FtsZ1-2 and 2-1 respectively. Black line represents a liner fit to the data points. i-l) Mean importance of structural features for the set of surrogate model predicting each mechanical parameter, i) $\bar{\sigma}$. j) $\bar{\epsilon}$. k) FR. l) FB. The orange line represents cumulative importance.

for the surrogate models (Fig. 8l).

4. Discussion

It is known that the structure and the functionality of cytoskeletal protein networks are deeply linked [11, 59, 60]. Although the biochemical aspect of these protein networks has been thoroughly studied, little is known about the interplay between the structural characteristics of these networks and their mechanical functionality. Here we proposed a data-driven approach to investigate the structure-function relationship in FtsZ protein network.

4.1. Mechanical Response of FtsZ Isoforms

We were able to show that the mechanical response of a protein network to external loads and that the precise structural response of FtsZ networks due to compression depend on the load direction and is different for FtsZ1-2 and FtsZ2-1 isoforms. This is to our knowledge the first detailed in silico investigation of the mechanical behaviour of cytoskeletal protein structures. It allows for a virtual assessment of sample-specific responses to applied loads. The identified isoform-specific mechanical responses support the assumption of potentially different structural roles of these two main FtsZ isoforms [23]. Further, the isoform-specific mechanical responses are in accordance with the functional- and morphological-related observations of these two isoforms in yeast cells [20, 21]. The dependency of the mechanical response with respect to the load direction might be related to the previously reported plate-like shapes of both isoforms, e.g., the negative oblateness as reported in Özdemir et al. [25].

With an increasing amount of compression, differences in the mechanical behavior of the two isoforms vanish (Fig 5c-f). This suggests that the isofroms contribute in response to large chloroplast deformation in a similar (or combined) fashion to the plastid mechanics. Moreover, FtsZ isoforms show a nonlinear increase in stress and strain with an increase in network deformation. This is similar to previously reported behavior of microtubule [61, 62] and actin filaments [63]. This points toward similar load-bearing functionality of FtsZ (as plastoskeleton). Furthermore, for compressions up to 20%, buckling remains the prevailing failure factor. The FB, which reaches its limit at about 1%, suggests that the network minimizes the buckling probability indicating an adaptive stability of FtsZ networks. Such a property was previously already suggested in [23, 64]. Although the rapture failure that steadily increases with increasing compression, it remains significantly lower than the bulking failure factor. This makes the rapture failure a less defining parameter for network failure. One reason for this might be the fact that FtsZ filaments experiencing high strain values lead to rapture only after buckling and at the location of bucking. This is similar to the fragmentation of buckled actin filaments [65].

Previous studies employing simplified geometries, such as tensegrity models allowed theoretical studies of cellular mechanism e.g. as cell reorientation [12, 16]. More detailed FE models have been developed to investigate the mechanical role of cytoskeletal components

[14] and cell mechano-sensitivity [66]. However, the generic and strongly simplified geometrical representation of the cells, e.g ellipsoid [67, 68] (even when cytoskeleton filament directions were considered), potentially prevents comprehensive studies of the influence of structural features in the mechanical behavior of cytoskeletal protein networks. Our approach of performing μFE simulations on segmented 3D network geometries of life networks allows one to analyse structure-related aspects of protein network mechanics. Further, investigating the sub-cellular components separated from their surrounding allows one to decouple protein network mechanics from whole cell mechanics. To date, contributions of cytoskeletal structures to whole cellular mechanics can up till now only be indirectly inferred from experimental techniques such as AFM [69] and optical tweezers [70]. However, since the mechanical behavior of a cellular structure is determined by many components, such as of the structure of the cortical, intra-cellular (non-cortical) cytoskeletal, and nuclear networks, as well as their distribution in space, decoupling the individual components remains challenging [14, 71, 72]. It has been suggested that AFM measurements with sharp tips tend to emphasize biomechanical properties of the cell cortex, whereas AFM measurements with round-tips tend to emphasize stiffness of the intra-cellular network [72]. Combing such measurements with a structural detailed models, as shown here, would possibly further advance the understanding of cellular mechanics.

4.2. Automatic Isoform Classification

Our ML-based end-to-end classification model trained on the extracted structural features achieved high accuracy (6 out of 7 correct prediction for all 8 models, average F1-score of 0.83). Moreover, our thorough validation step eradicated the dependency of classification results on dataset division. Analyzing the feature importance in the classification task reveals the structural features that contribute most to the classification. Four out of five of these distinguishing features also show significant different values in the two FtsZ isoforms [25], which confirms, that the model automatically extracts the distinguishing features. Our classification model achieved on par accuracy with deep learning based protein network classification methods [73, 74], while adding the ability of extracting specific structural features enabling the classification model to perform predictions. This may lead to a better understanding of biological network design concepts.

4.3. Structure-function Relationship in FtsZ Network

Our mechanical surrogate model is capable of predicting the mechanical behavior of protein networks in response to external loading. This holds for 2% as well as 20% compression ($0.69 \leq R^2 \leq 0.90$ and $0.97 \leq R^2 \leq 0.99$, respectively). However, the relatively higher accuracy for large network compression points toward higher correspondence of the extracted structural features to the mechanical behavior of the network in response to large deformations. This specifically coheres to the hypothesis that these networks are able to undergo large deformations without losing their structural integrity, as previously postulated [23]; hence, possessing structural features conforming to response in case of large deformations. The high accuracy in mapping the structural features to the mechanical behavior of the networks further demonstrates the potential load bearing functionality of FtsZ protein in

chloroplasts. Furthermore, this shows that the capability of the network to keep its stability by undergoing deformations relies not only on material properties of the biopolymer, but probably more prominently on the structural features of the network. This is in accordance with the effects of the network architecture on the overall mechanical behavior reported in actin protein network [75]. In summary, to our knowledge, this is the first detailed investigation of these sample-specific structure-based mechanical analysis of performance correlations. This enables us to not only have a image-based virtual mechanical testing method, but also a method to investigate the manifestation of the mechanical characteristics of structural network features.

By analyzing the importance of the features of the surrogate models in predicting stresses and strains of the network, we could show that the structural characteristics of the filaments (local changes of direction and thickness (I_S), average thickness (th_S) and open end filaments(N_{op})) as well as network overall morphology (network density (ρ_{PN}) and oblateness (Ob_{PN})) are the structural features mostly contributing to the large deformation mechanical response of the networks. This can be interpreted as the network being capable of stopping the increase in failure possibility because of buckling of its filaments by possessing an arrangement of the nodes and filaments with the specific architecture that includes: average node-to-node distance, d_{nn} in FtsZ1-2 and FtsZ2-1: $5.9\mu m$), local changes of direction and thickness of filaments ($I_S = 18.8$), the distance between the local changes of filaments ($d_{pp} = 60nn$) and number of filaments in the network ($N_S = 207$). This could potentially be used to design adaptively stable structures capable of undergoing large deformations [76] or mechanically optimized and synthetically engineered biomaterials [77, 78].

4.4. Limitations

Our study has also limitations. First, the imaging resolution might affect the simulation results as well as the mapping of the surrogate models. However, we have previously shown that our quantitative imaging method is capable of resolving the micro-structure of FtsZ networks [25]. Second, the commonly used linear elastic material model in FE simulations of cytoskeletons [14, 15, 66, 79] might not completely capture the mechanical behavior of the network. However, to our knowledge, to date no constitutive law has been developed for describing mechanical behavior of the FtsZ network. Although more complicated constitutive laws for the mechanical behavior of single actin filaments have been proposed [80–82], linear elasticity is the prevailing choice for cytoskeletal networks in whole-cell models [14, 15, 66, 79]. Moreover, our focus was not necessarily to exactly match the mechanical behaviour, but on the influences of structural features. Future studies should focus on combining our approach of precisely modeling the micro-structure with experimental techniques, such as atomic force microscopy, to further investigate material properties of the FtsZ-based plastoskeleton. Third, the loading conditions of our simulations are not an exact duplication of reality where a combination of active dynamic forces [45] as well as osmotic pressure [83] drive the morphological changes of the network. Moreover, the FtsZ isoform is surrounded by other proteins as well as other materials such as inter-organelle fluids. Our designed simulation setup provides a generic platform to investigate the structure-function relationships in FtsZ protein network rather than a one-to-one simulation of dynamics of

plastids. Finally, the failure criteria used in this study are experimentally derived from actin filaments [49, 84], since no failure criteria has been experimentally derived for FtsZ to date. However, due to the assumed similarity in structural functionality between the FtsZ network and actin networks and the similarity of rigidity in FtsZ and actin filaments, actin failure criteria might represent FtsZ behavior to a certain extent.

5. Conclusions

In this work, we showed that combing confocal microscopy imaging with μFE analysis employing a machine learning framework allows for an image-based surrogate model capable of predicting cellular mechanics. Additionally, by providing a way to identify structural features determining the mechanical response with respect to a given stimulus, we were able, for the first time, to directly investigate the structure-function relationship of individual protein networks in a sample-specific manner. Our ML surrogate model trained on in-silico data generates highly accurate and fast predictions of isoform classification prediction and the mechanical behavior on the sub-cellular level. Our method provides a framework to further investigate structural functionality of protein networks in plants as well as in humans. It allows to monitor the structure-function relationships of cytoskeletal components during morphological and, hence, time-dependent, changes, e.g., actin-driven cell shaping. This may also lead to am improved understanding of the mechanical aspects of cell-biomaterial interaction, and would provide the necessary insights into designing functionally optimal biomaterials. Further, cytoskeletal changes, which have been shown to occur in certain diseases, such as cancer and Alzheimer's disease could be more precisely quantified and, thus, more specifically target for future drug development.

Acknowledgements

This study was supported by the Deutsche Forschungsgemeinschaft (DFG, German Research Foundation) under Germany's Excellence Strategy – EXC 2075–390740016 (SimTech) and EXC 2189 (CIBSS), and as a part of Transregio/SFB TRR141, project A09.

Conflict of interest statement

All authors declare no conflicting interests.

Author's roles

Conceptualization: PA, AB, RR, and OR. Contributing software tools: PA. Data processing and analysis: PA and AB, ZT. Molecular biology and microscopy: BÖ. Writing - original draft: PA and AB. Writing - review and editing: All. Funding acquisition: RR and OR.

References

[1] M. A. Jordan, L. Wilson, Microtubules as a target for anticancer drugs, Nature Reviews Cancer 4 (2004) 253.

[2] C. A. Parent, Making all the right moves: chemotaxis in neutrophils and dictyostelium, Current opinion in cell biology 16 (2004) 4–13.

[3] E. W. Flitney, E. R. Kuczmarski, S. A. Adam, R. D. Goldman, Insights into the mechanical properties of epithelial cells: the effects of shear stress on the assembly and remodeling of keratin intermediate filaments, The FASEB Journal 23 (2009) 2110–2119.

[4] J. Guck, S. Schinkinger, B. Lincoln, F. Wottawah, S. Ebert, M. Romeyke, D. Lenz, H. M. Erickson, R. Ananthakrishnan, D. Mitchell, et al., Optical deformability as an inherent cell marker for testing malignant transformation and metastatic competence, Biophysical journal 88 (2005) 3689–3698.

[5] S. Suresh, J. Spatz, J. Mills, A. Micoulet, M. Dao, C. Lim, M. Beil, T. Seufferlein, Connections between single-cell biomechanics and human disease states: gastrointestinal cancer and malaria, Acta biomaterialia 1 (2005) 15–30.

[6] S. Suresh, Mechanical response of human red blood cells in health and disease: some structure-property-function relationships, Journal of materials research 21 (2006) 1871–1877.

[7] M. G. Mendez, S.-I. Kojima, R. D. Goldman, Vimentin induces changes in cell shape, motility, and adhesion during the epithelial to mesenchymal transition, The FASEB Journal 24 (2010) 1838–1851.

[8] C.-Y. Liu, H.-H. Lin, M.-J. Tang, Y.-K. Wang, Vimentin contributes to epithelial-mesenchymal transition cancer cell mechanics by mediating cytoskeletal organization and focal adhesion maturation, Oncotarget 6 (2015) 15966.

[9] J. Hendrick, M. Franz-Wachtel, Y. Moeller, S. Schmid, B. Macek, M. A. Olayioye, The polarity protein scribble positions dlc3 at adherens junctions to regulate rho signaling, J Cell Sci 129 (2016) 3583–3596.

[10] A. N. Ketene, E. M. Schmelz, P. C. Roberts, M. Agah, The effects of cancer progression on the viscoelasticity of ovarian cell cytoskeleton structures, Nanomedicine: Nanotechnology, Biology and Medicine 8 (2012) 93–102.

[11] D. A. Fletcher, R. D. Mullins, Cell mechanics and the cytoskeleton, Nature 463 (2010) 485.

[12] D. E. Ingber, Tensegrity: the architectural basis of cellular mechanotransduction, Annual review of physiology 59 (1997) 575–599.

[13] J. S. Milner, M. W. Grol, K. L. Beaucage, S. J. Dixon, D. W. Holdsworth, Finite-element modeling of viscoelastic cells during high-frequency cyclic strain, Journal of functional biomaterials 3 (2012) 209–224.

[14] S. Barreto, C. H. Clausen, C. M. Perrault, D. A. Fletcher, D. Lacroix, A multi-structural single cell model of force-induced interactions of cytoskeletal components, Biomaterials 34 (2013) 6119–6126.

[15] D. R. Katti, K. S. Katti, Cancer cell mechanics with altered cytoskeletal behavior and substrate effects: A 3d finite element modeling study, Journal of the mechanical behavior of biomedical materials 76 (2017) 125–134.

[16] G.-K. Xu, B. Li, X.-Q. Feng, H. Gao, A tensegrity model of cell reorientation on cyclically stretched substrates, Biophysical journal 111 (2016) 1478–1486.

[17] R. Reski, Rings and networks: the amazing complexity of ftsz in chloroplasts, Trends in plant science 7 (2002) 103–105.

[18] D. W. Adams, J. Errington, Bacterial cell division: assembly, maintenance and disassembly of the z ring, Nature Reviews Microbiology 7 (2009) 642.

[19] K. W. Osteryoung, K. A. Pyke, Division and dynamic morphology of plastids, Annual Review of Plant Biology 65 (2014) 443–472.

[20] A. D. TerBush, J. S. MacCready, C. Chen, D. C. Ducat, K. W. Osteryoung, Conserved dynamics of chloroplast cytoskeletal ftsz proteins across photosynthetic lineages, Plant physiology 176 (2018) 295–306.

[21] A. D. TerBush, K. W. Osteryoung, Distinct functions of chloroplast ftsz1 and ftsz2 in z-ring structure and remodeling, J Cell Biol 199 (2012) 623–637.

[22] K. W. Osteryoung, Conserved cell and organelle division, Nature 376 (1995) 473–474.

[23] A. Martin, D. Lang, S. T. Hanke, S. J. Mueller, E. Sarnighausen, M. Vervliet-Scheebaum, R. Reski, Targeted gene knockouts reveal overlapping functions of the five physcomitrella patens ftsz isoforms in chloroplast division, chloroplast shaping, cell patterning, plant development, and gravity sensing, Molecular plant 2 (2009) 1359–1372.

[24] P. Asgharzadeh, B. Özdemir, R. Reski, O. Röhrle, A. I. Birkhold, Computational 3d imaging to quantify structural components and assembly of protein networks, Acta Biomaterialia 69 (2018) 206–217.

[25] B. Özdemir, P. Asgharzadeh, A. I. Birkhold, S. J. Mueller, O. Röhrle, R. Reski, Cytological analysis and structural quantification of ftsz1-2 and ftsz2-1 network characteristics in physcomitrella patens, Scientific reports 8 (2018) 11165.

[26] A. Kan, Machine learning applications in cell image analysis, Immunology and cell biology 95 (2017) 525–530.

[27] P. Asgharzadeh, O. Röhrle, B. M. Willie, A. I. Birkhold, Decoding the rejuvenating effects of mechanical loading on skeletal maturation using in vivo imaging and deep learning, arXiv preprint arXiv:1905.08099 (2019).

[28] M. Masso, I. I. Vaisman, Accurate prediction of stability changes in protein mutants by combining machine learning with structure based computational mutagenesis, Bioinformatics 24 (2008) 2002–2009.

[29] P. Baldi, G. Pollastri, A machine learning strategy for protein analysis, IEEE Intelligent Systems 17 (2002) 28–35.

[30] F. Fritzen, M. Fernández, F. Larsson, On-the-fly adaptivity for nonlinear twoscale simulations using artificial neural networks and reduced order modeling, Frontiers in Materials 6 (2019) 75.

[31] J. D. Evans, F.-X. Coudert, Predicting the mechanical properties of zeolite frameworks by machine learning, Chemistry of Materials 29 (2017) 7833–7839.

[32] A. Hohe, R. Reski, Optimisation of a bioreactor culture of the moss physcomitrella patens for mass production of protoplasts, Plant Science 163 (2002) 69–74.

[33] S. Kircher, F. Wellmer, P. Nick, A. Rügner, E. Schäfer, K. Harter, Nuclear import of the parsley bzip transcription factor cprf2 is regulated by phytochrome photoreceptors, The Journal of cell biology 144 (1999) 201–211.

[34] A. Hohe, T. Egener, J. M. Lucht, H. Holtorf, C. Reinhard, G. Schween, R. Reski, An improved and highly standardised transformation procedure allows efficient production of single and multiple targeted gene-knockouts in a moss, physcomitrella patens, Current genetics 44 (2004) 339–347.

[35] G. Ofek, D. C. Wiltz, K. A. Athanasiou, Contribution of the cytoskeleton to the compressive properties and recovery behavior of single cells, Biophysical journal 97 (2009) 1873–1882.

[36] M. Zilske, H. Lamecker, S. Zachow, Adaptive remeshing of non-manifold surfaces, Proc. EUROGRAPHICS 27 (2008).

[37] F. Gittes, B. Mickey, J. Nettleton, J. Howard, Flexural rigidity of microtubules and actin filaments measured from thermal fluctuations in shape., The Journal of cell biology 120 (1993) 923–934.

[38] H. Felgner, R. Frank, M. Schliwa, Flexural rigidity of microtubules measured with the use of optical tweezers, Journal of cell science 109 (1996) 509–516.

[39] H. Felgner, R. Frank, J. Biernat, E.-M. Mandelkow, E. Mandelkow, B. Ludin, A. Matus, M. Schliwa, Domains of neuronal microtubule-associated proteins and flexural rigidity of microtubules, The Journal of cell biology 138 (1997) 1067–1075.

[40] L. D. Landau, E. M. Lifshitz, V. Berestetskii, L. Pitaevskii, Course of Theoretical Physics: Theory of Elasticity, 1995.

[41] I. Hörger, E. Velasco, J. Mingorance, G. Rivas, P. Tarazona, M. Vélez, Langevin computer simulations of bacterial protein filaments and the force-generating mechanism during cell division, Physical Review E 77 (2008) 011902.

[42] I. Hörger, E. Velasco, G. Rivas, M. Vélez, P. Tarazona, Ftsz bacterial cytoskeletal polymers on curved surfaces: the importance of lateral interactions, Biophysical journal 94 (2008) L81–L83.

[43] C. Lu, M. Reedy, H. P. Erickson, Straight and curved conformations of ftsz are regulated by gtp hydrolysis, Journal of bacteriology 182 (2000) 164–170.

[44] P. L. Navajas, G. Rivas, J. Mingorance, P. Mateos-Gil, I. Hörger, E. Velasco, P. Tarazona, M. Vélez,

In vitro reconstitution of the initial stages of the bacterial cell division machinery, Journal of biological physics 34 (2008) 237–247.

[45] D. J. Turner, I. Portman, T. R. Dafforn, A. Rodger, D. I. Roper, C. J. Smith, M. S. Turner, The mechanics of ftsz fibers, Biophysical journal 102 (2012) 731–738.

[46] H. P. Erickson, M. Osawa, Ftsz constriction force–curved protofilaments bending membranes, in: Prokaryotic Cytoskeletons, Springer, 2017, pp. 139–160.

[47] H. P. Erickson, D. W. Taylor, K. A. Taylor, D. Bramhill, Bacterial cell division protein ftsz assembles into protofilament sheets and minirings, structural homologs of tubulin polymers, Proceedings of the National Academy of Sciences 93 (1996) 519–523.

[48] H. Kojima, A. Ishijima, T. Yanagida, Direct measurement of stiffness of single actin filaments with and without tropomyosin by in vitro nanomanipulation, Proceedings of the National Academy of Sciences 91 (1994) 12962–12966.

[49] V. Rajagopal, W. R. Holmes, P. V. S. Lee, Computational modeling of single-cell mechanics and cytoskeletal mechanobiology, Wiley Interdisciplinary Reviews: Systems Biology and Medicine 10 (2018) e1407.

[50] H. Kubitschke, J. Schnauss, K. D. Nnetu, E. Warmt, R. Stange, J. Kaes, Actin and microtubule networks contribute differently to cell response for small and large strains, New Journal of Physics 19 (2017) 093003.

[51] P. A. Janmey, U. Euteneuer, P. Traub, M. Schliwa, Viscoelastic properties of vimentin compared with other filamentous biopolymer networks., The Journal of cell biology 113 (1991) 155–160.

[52] W. Pistoia, B. Van Rietbergen, E.-M. Lochmüller, C. Lill, F. Eckstein, P. Rüegsegger, Estimation of distal radius failure load with micro-finite element analysis models based on three-dimensional peripheral quantitative computed tomography images, Bone 30 (2002) 842–848.

[53] M. Pal, Random forest classifier for remote sensing classification, International Journal of Remote Sensing 26 (2005) 217–222.

[54] L. Breiman, Random forests, Machine learning 45 (2001) 5–32.

[55] W. Feller, An introduction to probability theory and its applications, volume 2, John Wiley & Sons, 2008.

[56] L. Breiman, J. Friedman, R. Olshen, C. Stone, Classification and regression trees. wadsworth int, Group 37 (1984) 237–251.

[57] F. Pedregosa, G. Varoquaux, A. Gramfort, V. Michel, B. Thirion, O. Grisel, M. Blondel, P. Prettenhofer, R. Weiss, V. Dubourg, J. Vanderplas, A. Passos, D. Cournapeau, M. Brucher, M. Perrot, E. Duchesnay, Scikit-learn: Machine Learning in Python , Journal of Machine Learning Research 12 (2011) 2825–2830.

[58] G. James, D. Witten, T. Hastie, R. Tibshirani, An introduction to statistical learning, volume 112, Springer, 2013.

[59] R. McBeath, D. M. Pirone, C. M. Nelson, K. Bhadriraju, C. S. Chen, Cell shape, cytoskeletal tension, and rhoa regulate stem cell lineage commitment, Developmental cell 6 (2004) 483–495.

[60] E. L. Elson, Cellular mechanics as an indicator of cytoskeletal structure and function, Annual review of biophysics and biophysical chemistry 17 (1988) 397–430.

[61] Y.-C. Lin, G. H. Koenderink, F. C. MacKintosh, D. A. Weitz, Viscoelastic properties of microtubule networks, Macromolecules 40 (2007) 7714–7720.

[62] Y. Yang, M. Bai, W. S. Klug, A. J. Levine, M. T. Valentine, Microrheology of highly crosslinked microtubule networks is dominated by force-induced crosslinker unbinding, Soft matter 9 (2013) 383–393.

[63] M. L. Gardel, K. E. Kasza, C. P. Brangwynne, J. Liu, D. A. Weitz, Mechanical response of cytoskeletal networks, Methods in cell biology 89 (2008) 487–519.

[64] P. Asgharzadeh, B. Özdemir, S. J. Müller, O. Röhrle, R. Reski, Analysis of physcomitrella chloroplasts to reveal adaptation principles leading to structural stability at the nano-scale, in: Biomimetic Research for Architecture and Building Construction, Springer, 2016, pp. 261–275.

[65] M. Enrique, J.-L. Martiel, L. Blanchoin, Mechanical heterogeneity favors fragmentation of strained actin filaments, Biophysical journal 108 (2015) 2270–2281.

[66] X. Yang, L.-W. Sun, C.-F. Du, X.-T. Wu, Y.-B. Fan, Finite element analysis of osteocytes mechanosensitivity under simulated microgravity, Microgravity Science and Technology (2018) 1–13.

[67] E. Gladilin, P. Gonzalez, R. Eils, Dissecting the contribution of actin and vimentin intermediate filaments to mechanical phenotype of suspended cells using high-throughput deformability measurements and computational modeling, Journal of biomechanics 47 (2014) 2598–2605.

[68] I. V. Pivkin, Z. Peng, G. E. Karniadakis, P. A. Buffet, M. Dao, S. Suresh, Biomechanics of red blood cells in human spleen and consequences for physiology and disease, Proceedings of the National Academy of Sciences 113 (2016) 7804–7809.

[69] M. Li, N. Xi, Y. Wang, L. Liu, Advances in atomic force microscopy for single-cell analysis, Nano Research 12 (2019) 703–718.

[70] M. Dao, C. T. Lim, S. Suresh, Mechanics of the human red blood cell deformed by optical tweezers, Journal of the Mechanics and Physics of Solids 51 (2003) 2259–2280.

[71] N. Curry, G. Ghézali, G. S. Kaminski Schierle, N. Rouach, C. F. Kaminski, Correlative sted and atomic force microscopy on live astrocytes reveals plasticity of cytoskeletal structure and membrane physical properties during polarized migration, Frontiers in cellular neuroscience 11 (2017) 104.

[72] A. Vahabikashi, C. Y. Park, K. Perkumas, Z. Zhang, E. K. Deurloo, H. Wu, D. A. Weitz, W. D. Stamer, R. D. Goldman, J. J. Fredberg, et al., Probe sensitivity to cortical versus intracellular cytoskeletal network stiffness, Biophysical journal 116 (2019) 518–529.

[73] O. Z. Kraus, B. T. Grys, J. Ba, Y. Chong, B. J. Frey, C. Boone, B. J. Andrews, Automated analysis of high-content microscopy data with deep learning, Molecular Systems Biology 13 (2017) 924.

[74] T. Pärnamaa, L. Parts, Accurate classification of protein subcellular localization from high-throughput microscopy images using deep learning, G3: Genes, Genomes, Genetics 7 (2017) 1385–1392.

[75] M. Enrique, M. L. Gardel, Actin mechanics and fragmentation, Journal of Biological Chemistry 290 (2015) 17137–17144.

[76] R. Reski, B. Özdemir, P. Asgharzadeh, A. Birkhold, O. Röhrle, The plastid skeleton: a source of ideas in the nano range, in: Biomimetics for Architecture. Learning from Nature, Birkhäuser, 2019, pp. 163–166.

[77] X. Li, R. Cui, L. Sun, K. E. Aifantis, Y. Fan, Q. Feng, F. Cui, F. Watari, 3d-printed biopolymers for tissue engineering application, International Journal of Polymer Science 2014 (2014).

[78] X. Liu, H. Yuk, S. Lin, G. A. Parada, T.-C. Tang, E. Tham, C. de la Fuente-Nunez, T. K. Lu, X. Zhao, 3d printing of living responsive materials and devices, Advanced Materials 30 (2018) 1704821.

[79] S. Deguchi, T. Ohashi, M. Sato, Tensile properties of single stress fibers isolated from cultured vascular smooth muscle cells, Journal of biomechanics 39 (2006) 2603–2610.

[80] G. A. Holzapfel, R. W. Ogden, On the bending and stretching elasticity of biopolymer filaments, Journal of elasticity 104 (2011) 319–342.

[81] J. Blundell, E. Terentjev, Stretching semiflexible filaments and their networks, Macromolecules 42 (2009) 5388–5394.

[82] M. J. Unterberger, K. M. Schmoller, A. R. Bausch, G. A. Holzapfel, A new approach to model cross-linked actin networks: multi-scale continuum formulation and computational analysis, Journal of the mechanical behavior of biomedical materials 22 (2013) 95–114.

[83] J. M. Glynn, S.-y. Miyagishima, D. W. Yoder, K. W. Osteryoung, S. Vitha, Chloroplast division, Traffic 8 (2007) 451–461.

[84] Y. Wang, J. Qian, Buckling of filamentous actin bundles in filopodial protrusions, Acta Mechanica Sinica (2019) 1–11.